6th Edition of the European Conference on Supercritical CO2 (sCO2) for Energy Systems
April 09-11, 2025, Delft, Netherlands

2025-sCO2.eu-213

NUMERICAL INVESTIGATION OF HEADER DESIGN PARAMETERS FOR ENHANCED FLOW DISTRIBUTION IN MINICHANNEL PRINTED CIRCUIT HEAT EXCHANGERS FOR SUPERCRITICAL CARBON DIOXIDE APPLICATIONS

Ahmad Ali Awais*
University of Stuttgart
Stuttgart, Germany
Ahmad.awais@ike.uni-stuttgart.de

Markus Hofer
University of Stuttgart
Stuttgart, Germany
markus.hofer@ike.uni-stuttgart.de

Michael Buck
University of Stuttgart
Stuttgart, Germany
michael.buck@ike.uni-stuttgart.de

Sarah Tioual-Demange
FIVES Cryo
Golbey, France
sarah.tioual@fivesgroup.com

Jörg Starflinger
University of Stuttgart
Stuttgart, Germany
joerg.starflinger@ike.uni-stuttgart.de

ABSTRACT

Minichannel printed circuit heat exchangers (PCHEs) are commonly utilized in supercritical CO_2 (sCO_2) power cycles. In this study, an experimental single plate PCHE with various header configurations is investigated in terms of flow maldistribution using computational fluid dynamics (CFD) techniques. A series of header optimization simulations with different mass flow rates, inlet/outlet configurations, and header sizes are performed and analyzed. The numerical model of this PCHE is set up and solved with ANSYS-CFX. The variation in thermophysical properties of sCO_2 was incorporated into the numerical model via real gas property data. Additionally, the computed results for temperature distribution i.e., maximum hotspot temperatures and pressure drop were validated with experimental data, showing a good agreement with a maximum discrepancy of 8.6%. The results from this study indicated that optimizing inlet and outlet positions reduced the maldistribution factor (MDF) by 34% at 40 g/sec and 29% at 90 g/sec, as compared to the baseline configuration of the PCHE. Increasing the header area ratio further reduced the MDF by 51% at 40 g/sec and 48% at 90 g/sec, resulting in uniform temperature distribution and effective mitigation of local hotspots. Furthermore, the suggested header configuration also minimized hot and cold stream mixing inside the collector header which can significantly reduce thermal stresses, extending the life span of PCHEs.

INTRODUCTION

Recuperators and pre-coolers are critical components of thermal cycles such as supercritical CO_2 (sCO_2)-Brayton cycles. Their size and performance can greatly affect the efficiency of the overall power cycle. Printed Circuit Heat Exchangers (PCHEs) are widely used as recuperators in sCO_2 power cycles owing to their compactness, heat removal, and high-pressure capabilities [1]. In PCHEs, mini or microchannel plates are arranged in the longitudinal direction of the heat exchanger with distributor and collector headers at each end to serve as inflow and outflow for the working fluid throughout the heat exchanger. The design of the distributor header in PCHEs is important to ensure uniform flow throughout the PCHE. The non-uniformity in the flow of working fluid passing through the various channels of the PCHE is termed as flow maldistribution [2], which substantially reduces its thermal and hydraulic performance. Moreover, flow maldistribution can cause high thermal stress and overheating of regions. i.e. local hotspots within a PCHE which may lead to its failure. Therefore, this problem requires careful consideration of the geometrical aspects of the distributor header. These parameters should be investigated to minimize the flow maldistribution in PCHEs.

Currently, a number of researchers have studied the thermohydraulic performance of PCHEs. Apart from conventional straight pipes or channels [3], zigzag (wavy) channels [4], discontinuous S-shape channels [5], airfoil-shaped channels [6], and C-shaped channels [7], [8] have also been suggested. In the case of sCO_2 power cycles, straight-channel PCHE could be favored as they are less complex to manufacture and have lower pressure drops [9]. Hence, the current research is focused on PCHE using straight channels. Similarly, flow maldistribution has been investigated in various studies. Wen et al. [10], presented a study involving the investigation of inlet flow distribution characteristics of plate-fin heat exchangers using particle image velocimetry (PIV) technology. It was shown that substantial flow non-uniformity is observed at the conventional inlet. Kim [11] was able to optimize the header design through explicit optimization algorithms, a 3D computational fluid dynamics (CFD) method, and other design modifications. Their efforts resulted in a 7.8% increase in the efficiency of heat transfer over the baseline header design. Tereda et al.[12] studied the pressure drop across a PCHE with U-type and Z-type inlet and outlet port configurations using water as the working fluid. They concluded the effect of header inlet and outlet diameters can significantly affect the flow distribution in plate heat exchangers. Wang's experimental model [13] was employed by Camilleri et al. [14] to establish a

* corresponding author(s)

DOI: 10.17185/duepublico/83329

This work may be used under a Creative Commons Attribution 4.0 License.

framework for predicting flow distribution. Their parameter sensitivity analysis showed that the ratio of the area of the channel to the area of the manifold has an important impact on the flow maldistribution. Hence, the effect of header area ratio (HAR) on flow maldistribution is also considered in this study.

Regarding PCHEs using sCO_2 as the working fluid, only a few studies address the issue of maldistribution. Chu et al. [15] investigated different header configurations and suggested that hyperbolic header design can reduce the flow non-uniformity by 46% as compared to conventional header design. In contrast, Saeed et al. [16] studied different header shape profiles i.e., triangular, rectangular, and hyperbolic header shapes for a microchannel heat exchanger using sCO_2 near the critical point. Their results showed that significant maldistribution was present for all header shapes. Recently, Jin et al. [17] compared the effect of free manifold and straight ribbed manifold design on flow maldistribution for different channel shapes. They highlighted in their research that the study of flow characteristics inside the distributor header is critical to reducing flow maldistribution. The above discussion suggests that only scarce literature is available investigating the impact of inlet and outlet configuration on flow maldistribution in PCHEs using sCO_2 near its critical point. Therefore, the current study aims to address this research gap by employing the Computational Fluid Dynamics (CFD) technique to investigate flow distribution inside a PCHE. For this purpose, real gas property (RGP) data in tabular format was supplied to ANSYS-CFX to accurately integrate the property variations of sCO_2 into the numerical model. Additionally, the numerical model was validated with experimental data. Afterward, the effects of inlet and outlet positions and header area ratio on flow maldistribution and base temperature distribution are reported. Furthermore, this study also provides valuable insights into the flow characteristics of sCO_2 inside the PCHE channels and headers.

GEOMETRICAL DETAILS

This study demonstrates the numerical optimization of the distributor header and collector configuration for an experimental sCO_2 minichannel PCHE, which was tested at the Supercritical Carbon Dioxide Loop at IKE Stuttgart (SCARLETT) [18]. This PCHE consists of a single plate made of steel with 50 straight minichannels with fin spacing and a fin thickness (t_f), fin height (h_f) of 2 mm each. The distributor and collector headers for the minichannel PCHE had three inlet and outlet openings with the diameter (ϕ) of 10 mm each for the inflow and outflow of the coolant. Further geometrical details of the PCHE are provided in Figure 1. In this numerical study, a heat load of 1300 W was applied at the base of the heat exchanger to simulate the electrical heating in the experiment. Then, the resulting temperature distribution and velocity profiles inside the channel for flow distribution were analyzed. Additionally, the effect of different configurations was compared with the experimental baseline configuration, and inlet and outlet distance from the side wall and header area ratio (HAR) were considered in this study. Details of various configurations of single-plate PCHE are enlisted in the Table. 1.

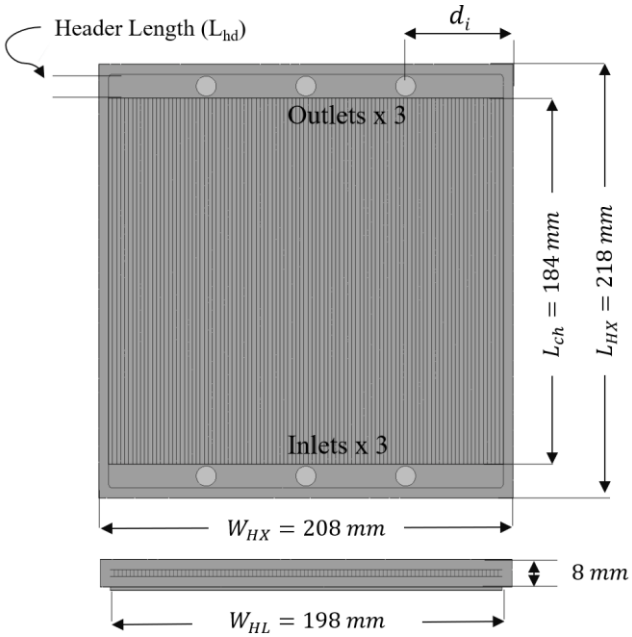

Figure 1: Geometrical details of single plate PCHE

Table. 1 Different configurations considered in this study

Header Configurations	Wall distance of side inlet (d_i) [mm]	Header length (L_{hd}) [mm]	Header area ratio (HAR) [%]
A	53	12	6
B	47	12	
C	43	12	
D	43	20	10

NUMERICAL MODEL

A steady and compressible form of RANS equation is employed to compute the conjugate heat transfer problem for sCO_2 using Eq. (1-4) [19] for the fluid domain and an energy equation for the solid domain (Eq. 5) via ANSYS-CFX [20]. The current study is performed based on the following assumptions: (1) the model neglects the effects of gravity on the fluid; (2) the exchanger's walls, base and top are considered adiabatic; (3) thermal resistance was considered negligible between PCHE base and heat load (4) Interface contact loss is neglected for fluid-solid domains.

Continuity, Momentum and Energy Equations for Fluid Domain

$$\nabla.\rho\mathbf{V} = 0 \tag{1}$$

$$\nabla.(\rho\mathbf{V}\otimes\mathbf{V}) = -\nabla p + \nabla.\boldsymbol{\tau} \tag{2}$$

DOI: 10.17185/duepublico/83329

The stress tensor ($\boldsymbol{\tau}$) for turbulent flow is defined below:

$$\boldsymbol{\tau} = (\mu + \mu_t)\left(\boldsymbol{\nabla V} + (\boldsymbol{\nabla V})^T - \frac{2}{3}\delta\boldsymbol{\nabla}.\mathbf{V}\right) = \mu\left(\boldsymbol{\nabla V} + (\boldsymbol{\nabla V})^T - \frac{2}{3}\delta\boldsymbol{\nabla}.\boldsymbol{V}\right) + \boldsymbol{\nabla}.\boldsymbol{\Pi} \quad (3)$$

In the equation above, "$\boldsymbol{\Pi}$" represents the Reynolds stress tensor.

$$\boldsymbol{\nabla}.(\rho \mathbf{V} H) = \boldsymbol{\nabla}.\left(\frac{\lambda + \lambda_t}{C_p}\boldsymbol{\nabla} h\right) \quad (4)$$

Energy Equation for Solid Domain

$$k_{sl}\,\nabla^2 T = 0 \quad (5)$$

Whereas the conjugated heat transfer at the fluid-solid interfaces is governed by Eq. (6).

$$\begin{aligned} \mathbf{V} &= 0 \\ T_{sl} &= T_{fl} \\ k_{sl}\frac{\partial T_{sl}}{\partial S_n} &= k_{fl}\frac{\partial T_{fl}}{\partial S_n} \end{aligned} \quad (6)$$

Heat load area at the base plate received a continuous heat flux of 1300 W, as computed by Eq. (7). Adiabatic boundary wall conditions are applied by Eq. (8) for fluid and solid domains.

$$Q_b = -\frac{k\partial T_{sl}}{\partial S_n} = -\frac{1300}{A_p} \quad (7)$$

$$\frac{\partial T_{sl}}{\partial S_n} = 0 \quad (8)$$

DOMAIN DISCRETIZATION AND MESH INDEPENDENCE STUDY

The present study focuses on channel geometries with a small hydraulic diameter, making accurate calculations of boundary layer thickness. In the literature, $K-\epsilon$ and shear stress transport (SST) turbulence models are widely popular among the researchers [21],[22]. Standard $K-\epsilon$ model offers more robustness and requires less computational power [23]. However, it only employs standard wall functions to model the flow characteristics [20] and it is unable to resolve the boundary layer. Therefore, numerous studies [24], [25], [26], [27] have already employed the SST turbulence model for different channel geometries of PCHEs [28]. These studies effectively utilized supercritical CO_2 as a working fluid based on research conducted by Van Abel et al [29]. To ensure the SST turbulence model was utilized to its maximized capabilities, y-plus (y^+) values were maintained below 1, and a minimum of 10 elements were used in the boundary layer thickness of the channels for the present study.

The discretization of fluid and solid domains was performed in ICEM-CFD utilizing structural blocking and hexahedral mesh elements while ensuring identical topologies and one to one ratio node connections for fluid and solid domain interfaces. To ensure mesh independence from the mesh size, three distinct mesh configurations as shown in Table 2 (M1 to M3) were employed for this study.

Table 2: Mesh Independence study

Configurations	Element count			Y Plus value	Base Temperature	Pressure Drop	RAM Allocation
	E_x	E_y	E_z	y^+	T_b [K]	ΔP [Pa]	[MB]
M1	20	20	460	1.05	306.62	5390.49	57674
M2	30	30	460	0.83	307.57	5780.12	81641
M3	40	40	460	0.61	307.29	5936.88	117153

For the current study, the parallel processing functionality available in CFX-solver was utilized to execute the simulations on a workstation equipped with 32-core processor. The total simulation time varied between 4 to 6 hours for different cases of boundary conditions. To choose the best mesh configuration, several parameters such as base temperature (T_b), pressure drop (ΔP), time to complete an iteration and allocation of system memory are compared as shown in Table 2 and Figure 2. The element counts E_x and E_y were gradually increased to improve the boundary layer resolution by reducing y^+ inside the channels. The comparison of high-resolution meshes, i.e., M2 and M3, shows only a minor difference in computed values of pressure drop (ΔP) and base temperatures (T_b). Specifically, the differences are 2%, and 0.04%, respectively. Hence, M3 was finalized for the current study. The finalized mesh configuration (M3) and mesh view for different configurations (M1 to M3) for mesh independence study are shown in Figure 3.

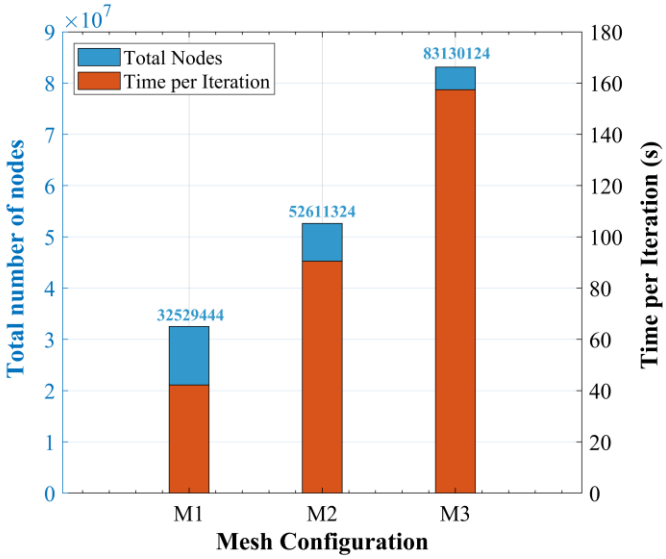

Figure 2: Computation time and nodal count for different mesh configurations

DOI: 10.17185/duepublico/83329

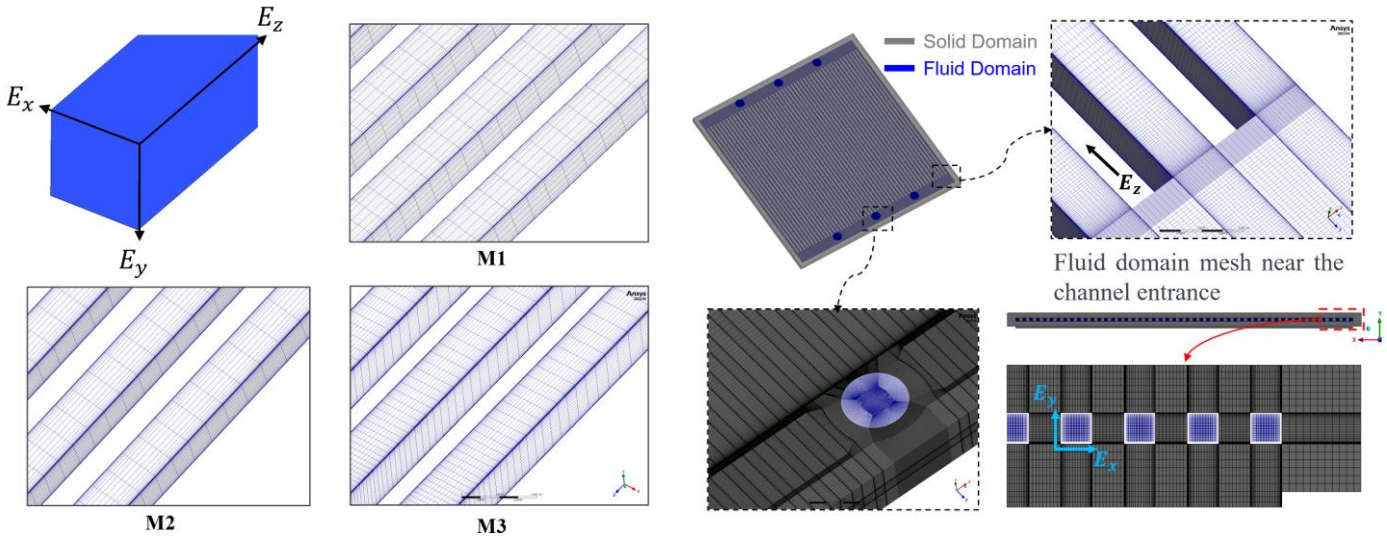

Figure 3: Different mesh configurations considered for the study (Right) and finalized meshes of fluid and solid domains (Left)

IMPLEMENTATION OF CO_2 PROPERTIES AND MODEL VALIDATION

Thermophysical properties of sCO_2 exhibit a high sensitivity to the variations in temperature and pressure near the critical point. Therefore, the changes in the thermophysical properties of sCO_2 should be precisely implemented in ANSYS-CFX to ensure that the computed results are accurate. The precise integration of the properties in ANSYS-CFX is possible through either an Equation of State (EoS) or Real Gas Property (RGP) table. Implementing properties through an EoS is computationally very expensive [30], [31]. Hence, to incorporate changes in the thermophysical characteristics of CO_2, ANSYS-CFX makes use of a specifically formatted high-resolution RGP file. The RGP file is produced using an in-house developed code that required linking MATLAB with the library data of NIST's REFPROP [32]. The Real gas property file is written in tabular format with a resolution of 600×800 for temperature and pressure ranges of $300-360\,K$ and $7.98-8.02$ MPa, respectively.

Figure 4 represents the variation of specific heat capacity of CO_2 at various channel locations AA', BB' and CC'. The trends show that the c_p is highly susceptible to the localized temperature variation inside the channels at different locations across the width of the printed circuit heat exchanger. Additionally, the value of c_p significantly increases as the CO_2 flows from channel entrance to channel exit which highlights the importance of incorporating of these property variations in the numerical model.

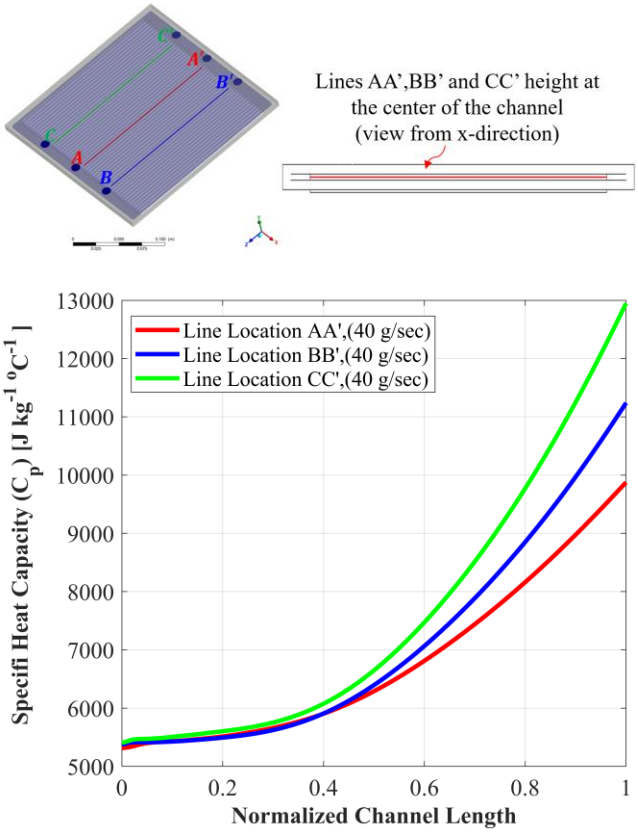

Figure 4: Variation of specific heat capacity (c_p) of sCO_2 along the different channel length locations in PCHE

DOI: 10.17185/duepublico/83329

Model Validation

As discussed in previous sections of the paper, the computed values of pressure drop and temperature distribution of the single plate PCHE were compared against the experimental data from the SCARLETT facility at IKE, University of Stuttgart. The heat load of 1300W in the experiment was applied using a copper block with dimensions of 198mm x 184mm using cartridge heaters. Whereas, for current simulation heat flux equivalent to the 1300W was applied as heat flux (see Eq. (7)) to the finned area at base of the PCHE as shown in Figure 5(a). The temperature distribution for the baseline configuration of PCHE (Configuration A) was visualized at the SCARLETT facility using a thermal camera as shown in Figure 5 (b). Whereas the temperature distribution computed using the current numerical model is shown in Figure 5 (c). The comparison of temperature gradients such as local hotspot temperature and hotspot locations between the experimental thermal camera image and computed distribution shows a close agreement. The difference between the numerically computed and experimentally observed values of local hotspot temperatures shows relatively good agreement except for some non-symmetrical effects. These localized discrepancies can be attributed to the non-homogeneous heat transfer from cartridge heaters in experiments and the thermal camera image plane can be misaligned from the actual PCHE base in the experimental study.

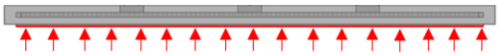

(a). Location of heat load area ($A_{HL} = 198\,mm \times 184\,mm$)

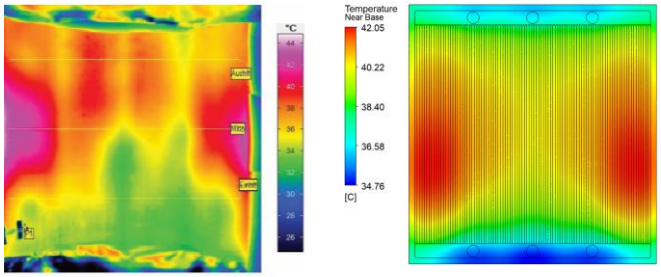

(b). Thermal camera image (c). Current numerical model

Figure 5: Comparison of temperature distribution from the numerical model with experimental results at 1300 W heat load

Furthermore, pressure drop was also compared at different values of mass flow rate. However, it should be mentioned that, for pressure drop comparison no heat load was applied to the PCHE base, and inlet pressure was also fixed at 7.5 MPa. For this purpose, a separate RGP file was generated to cover the pressure variation range using the method discussed previously. When observing pressure loss presented in Figure 6, it can be stated that the simulated results correlate well with the experimental ones in the entire range of mass flow rates (40 – 90 g/s). The maximum discrepancy between the values of parameters obtained through simulation and those obtained in the experiment does not exceed 8.6%. This agreement verifies the reliability of the numerical model to compute the flow mechanics at the given conditions accurately. It should also be noted here that the discrepancy in the pressure drops can partially be attributed to the measuring locations for the experimental data. For the simulation case, the pressure drop is measured as the difference of the average values of pressure between inlets and outlets. However, in the case of the experimental environment, the measuring location is slightly downstream or upstream of the inlet and outlet. Hence, this factor can contribute to the observed discrepancy values in case of pressure drop measurements.

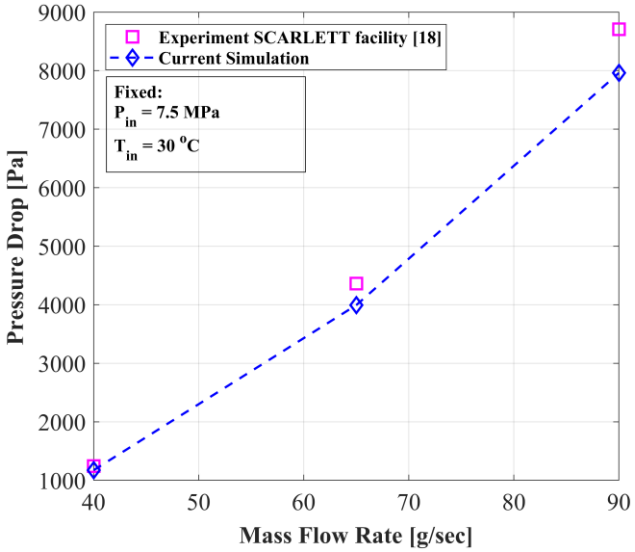

Figure 6: Comparison of pressure drop as a function of mass flow rate between numerical results and experimental data from the SCARLETT test facility

RESULTS & DISCUSSION

As discussed earlier, this study considers the experimental PCHE as the baseline configuration i.e., Configuration A (as used in the SCARLETT experiment). The effect of inlet positions i.e., Configuration B and Configuration C on flow maldistribution and temperature distribution is compared with baseline Configuration A. Furthermore, the impact of the header area ratio increased from 6% to 10% i.e., Configuration D is also compared to the respective performance parameters. The operating conditions were the same for all the configurations provided in Table. 3

Table. 3 Operating conditions for different configurations

Parameter	Value
Inlet Pressure (P_i)	8.0 MPa
Inlet Temperature (T_i)	30°C
Heating load at the base	1300W
Mass flow rate	40 g/sec, 90 g/sec

Figure 7 represents the location of different lines used for post-processing of different data sets computed in this numerical

DOI: 10.17185/duepublico/83329

study. The velocity distribution profiles have been provided with line DD' which passes through the mid-height of all the channels while line EE', which is located at the center of the base plate, has been used to show the respective temperature distribution profiles. Furthermore, line positions AA', BB', and CC' are employed in this research as part of the more comprehensive detail on sCO_2 flow dynamics inside the channel length at respective locations.

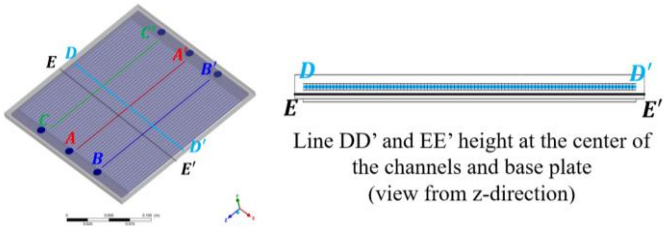

Figure 7: Different line locations for data plots

The effect of flow maldistribution on the temperature distributions within the baseline configuration (Configuration A) of the PCHE at mass flow rates of 40 g/sec and 90 g/sec are illustrated in Figure 8. The velocity distribution at the location of line DD' across the width of the PCHE shows significant flow maldistribution. Velocity distribution trends in Figure 8(a) show sharp velocity peaks at the center of PCHE while significant troughs in velocity values can be observed at the sides of the PCHE at employed mass flow rates of 40 g/sec and 90 g/sec. Figure 8(a) also illustrates that the channels near the inlet ports receive significantly higher mass flows whereas the channel at the side of the PCHE are underutilized due to inadequate supply of the fluid. Hence, non-unform distribution of fluid across the PCHE significantly reduces its thermal efficiency and leads to generating localized hotspots at the sides as shown in Figure 8(b). The temperature contours for 90 g/sec in the PCHE are visualized in Figure 8b, where temperature hotspots are observed in the regions around the sides of the PCHE, which corresponds to areas of lower flow velocities, and a drop in temperature in the center zone owing to high flow velocities. This effect is quantitatively presented along the line EE' in Figure 8(c) at 40 g/sec exhibiting a higher hotspot temperature of about 41.6°C. On the other hand, at 90 g/sec, the corresponding hotspot temperature reduces to around 38.8°C. Despite the reduction in the hotspot temperature at higher mass flow rate, maldistribution of similar degree remains evident in baseline configuration A. However, the Figure. 8 (c) shows that the temperature difference between hotspots and the PCHE center is higher at 90 g/sec. The enhanced convective heat transfer at a higher mass flow rate amplifies these temperature deviations. Hence, the effect of inlet and outlet positions on header configurations is investigated to address the non-uniform temperature distribution caused by uneven heat transfer dynamics resulting from flow maldistribution.

Figure 9 highlights the effect of channel entrance losses on flow dynamics such as Re variation alongside the channel length of PCHE at line locations AA', line BB', and line CC'. In addition, the effect of channel exit velocity on the collector header area is also discussed. Figure. 9(a) illustrates that Re changes abruptly at the channel entrance as a result of the inlet position and small header area ratio. As the working fluid i.e., supercritical carbon dioxide (sCO_2) enters the distributor header, it experiences abrupt changes in flow direction with respect to the PCHE's inlet leading to entrance losses which is clear from the distorted velocity vectors and velocity contours as shown in Figure 9(a). Another factor that contributes to the velocity losses is the positioning of the inlet next to the entrance of channels creating dead zones and consequently decreasing the active flow area. In the early stages of flow development, there is a significant rise in the Reynolds number along the channel length. For example, in Figure 9(a) it is observed that Re increases dramatically and reaches a value as high as 17,000 at near the channel exit at a mass flow rate of 40g/sec. The sharp rise in Re in value also corresponds to the high velocities at the exits of the channels, which in turn causes concentrated streams of jets within the collector header. The increased channel exit velocities cause flow stagnation and recirculation regions inside the collector header as shown in Figure 9(b). These disturbances in flow cause an effective reduction in the effective area of the

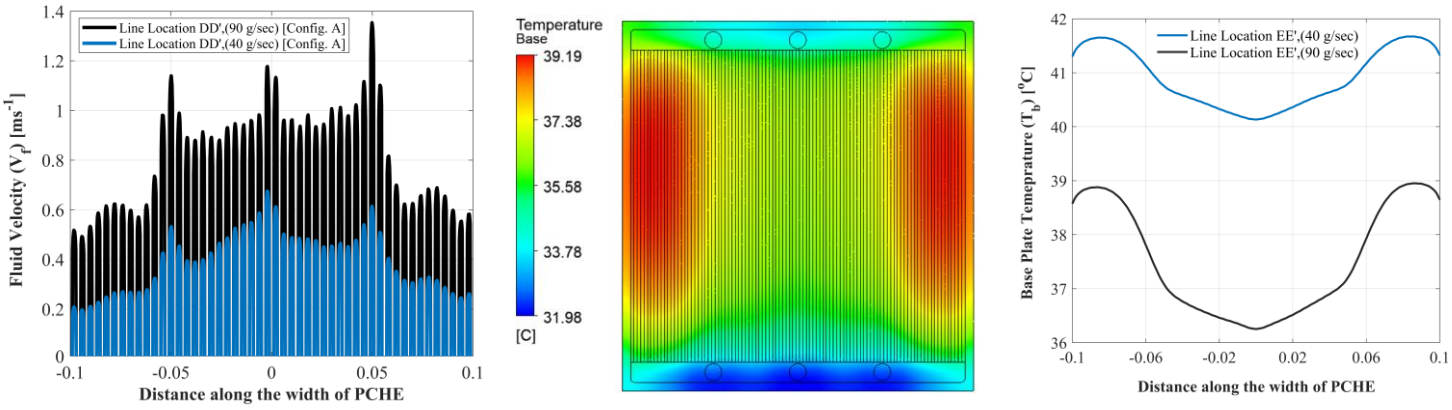

(a). Flow distribution in PCHE channels

(b). Temperature contours at PCHE base (90 g/sec)

(c). Temperature distribution at the PCHE base

Figure 8: Effect of flow maldistribution inside the PCHE on temperature distribution at mass flow rates of 40 g/sec and 90 g/sec

DOI: 10.17185/duepublico/83329

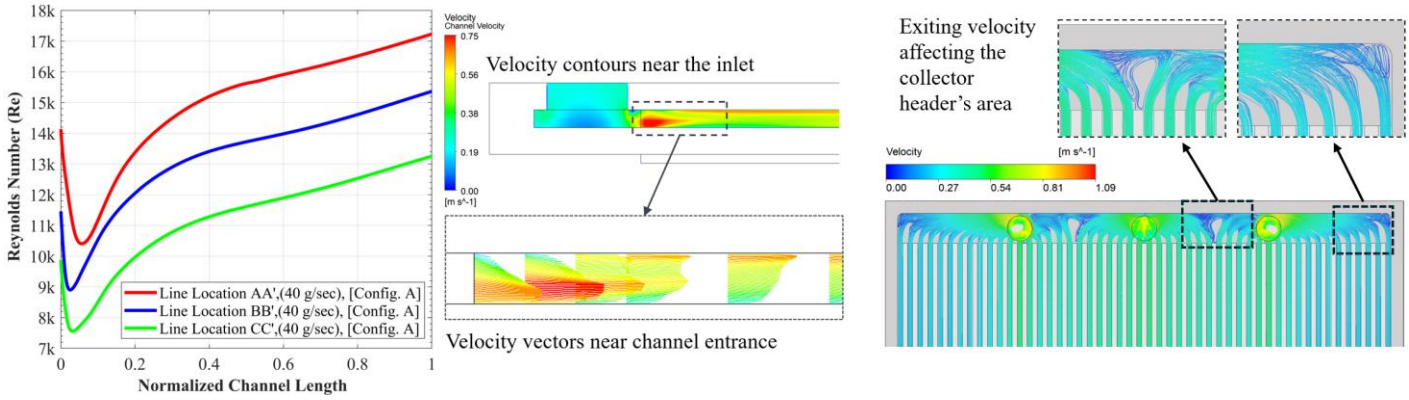

Figure 9: Effect of channel entrance losses on Re (a) and exit velocity on collector header area (b)

collector header side which eventually results in uneven pressure drops in adjacent channels leading to the high degree of flow maldistribution in PCHE. The results highlight the fact that the entrance loss and the reduction in the effective flow area of the collector header are important aspects to be considered while designing inlets and finalizing header area ratios for a specific PCHE. By increasing the header area ratio, some of these challenges can be addressed by ensuring smooth flow transitions at the channel entrance and exit.

The Maldistribution Factor (MDF) is defined as a dimensionless parameter that characterizes the non-uniformity of the velocity distribution of a (PCHE). It is expressed as the ratio of the standard deviation of channel velocities to the mean channel velocity in Eq. 9.

$$MDF = \sqrt{\frac{1}{N}\sum_{N}^{i}\frac{(v_i - \bar{v})^2}{\bar{v}}} \quad (9)$$

Here, v_i is the velocity in i^{th} channel and $\bar{v}$ is the mean channel velocity.

MDF values for four configurations (see Table. 1) are shown in Figure 10, in terms of modifications to the inlet-to-wall distance and header length or header area ratios (HAR). The configuration A is the baseline case, and it has a wall distance of 53 mm from the side inlets/outlets and a 12 mm header length which corresponds to a HAR of 6%. For configurations B and C, the inlet-to-wall distance is reduced to 47 mm and 43 mm respectively while keeping the HAR same as configuration A. Configuration D combines the reduction of inlet-to-wall distance to the value of 43 mm with an increase in the length of the header to 20 mm which resulted in a HAR of 10% for both distributor and collector header sides. The MDF values for each configuration for mass flow rates of 40 g/sec and 90 g/sec are presented in Figure 10. Configuration A reached the highest MDF values (0.302 at 40 g/sec and 0.265 at 90 g/sec), which means this configuration has significantly higher flow maldistribution. When the inlet-to-wall distance is reduced in configurations B and C, the flow becomes more uniform as depicted by the low MDF values. Configuration B decreases MDF by 26.82% (40 g/sec) and 20.75% (90 g/sec) when compared to configuration A, configuration C on the other hand made additional reductions of 34.11% and 29.06% for 40 g/sec and 90 g/sec respectively. Configuration D, with the increased header area ratio, shows the lowest MDF values (0.148 at 40 g/sec and 0.137 at 90 g/sec), as flow maldistribution is reduced by 50.99% and 48.30% over baseline configuration A at corresponding mass flow rates. From these results, it can be deduced that there is a significant merit in increasing the header area ratio to reduce the flow maldistribution.

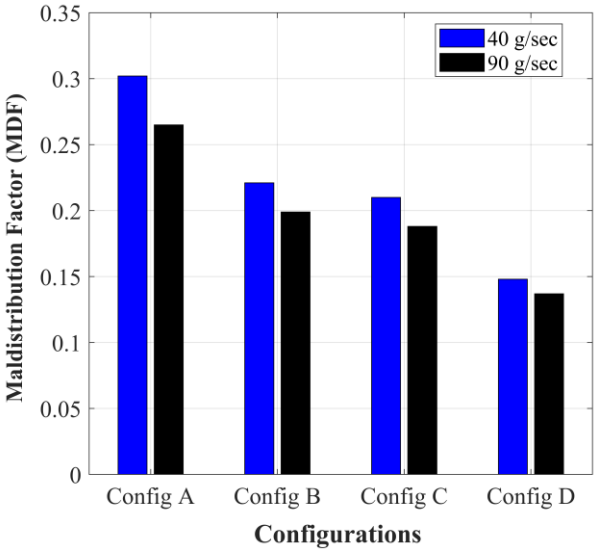

Figure 10: Comparison of Maldistribution Factor (MDF) for different header configurations and mass flow rates

Figure. 11 shows a visual representation of MDF for various header configurations at a mass flow rate of 90 g/sec, thus demonstrating the effectiveness of the design changes aimed at reducing flow maldistribution. Figure 11(a) depicts the velocity distribution of Configuration A which shows significant flow maldistribution confirming the poor performance of baseline Configuration A. On the other hand, Figure 11(b) for Configuration B depicts a significant reduction in

DOI: 10.17185/duepublico/83329

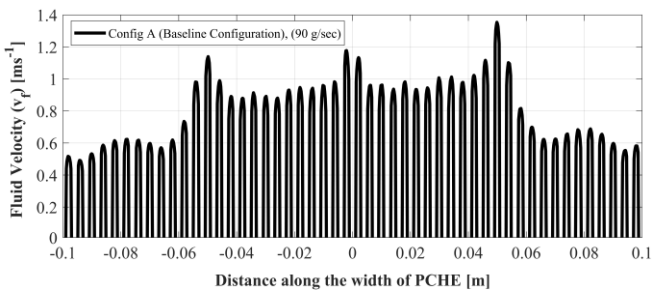

(a). Configuration A (Baseline configuration)

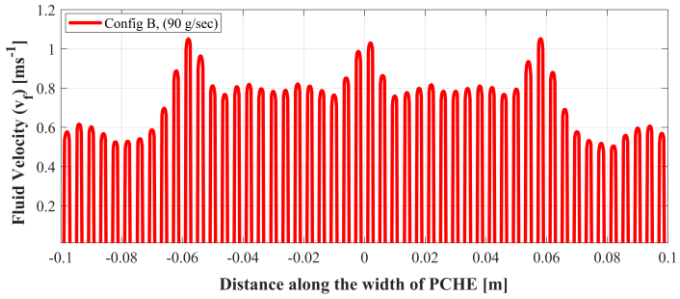

(b). Configuration B

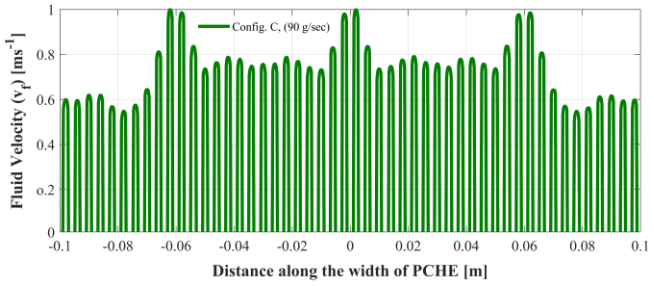

(c). Configuration C

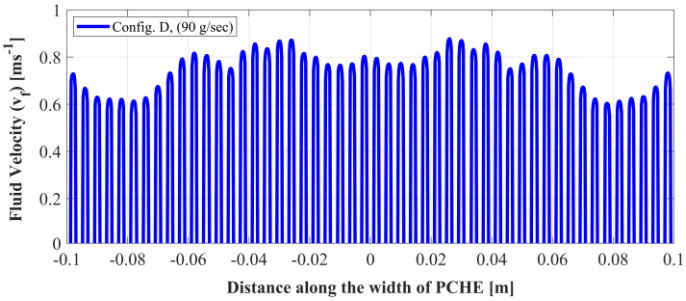

(d). Configuration D

Figure 11: Effect of different inlet configurations and header area ratio (HAR) on velocity distributions inside the channels.

maldistribution in comparison to Configuration A, which signifies the effect of inlet position on MDF. Similarly, for configuration C in Figure 11(c), it can be observed that the flow uniformity across the PCHE width is further enhanced. In the end, it is evident from Figure 11 (d) that Configuration D is the best configuration. The velocity profile is also the most uniform for Configuration D with minimal velocity variations across the width of the PCHE. This uniformity is realized by the combination of reduced inlet-to-wall distance as well as increased header area ratio which promotes better and smooth transition of flow momentum inside the distributor header.

Figure 12 shows the velocity streamlines in the distributor headers for Configuration A and Configuration D, highlighting the impact of header design on flow distribution. In Configuration A, strong recirculation zones and stagnation regions are observed within the distributor, as shown in Figure 12(a). These flow irregularities arise due to the smaller header area, which causes a more abrupt transition of flow from the header to the channels. The close proximity of the channel entrances to the inlet results in higher entrance losses and uneven mass flow distribution among the channels. This leads to increased velocity fluctuations and localized pressure variations, contributing to higher maldistribution factor (MDF) values. In contrast, Configuration D exhibits smoother velocity streamlines, as illustrated in Figure 12(b). The increased header size allows for better flow redistribution before the fluid enters the channels, reducing abrupt directional changes and minimizing entrance losses. By increasing the header-to-channel distance, the flow undergoes a more gradual transition, leading to a more uniform velocity distribution across the channel inlets. This improvement ensures better utilization of the distributor header area, reduces velocity fluctuations, and enhances overall flow uniformity. As a result, Configuration D achieves a lower MDF value, demonstrating the effectiveness of optimizing header design to mitigate maldistribution and entrance losses

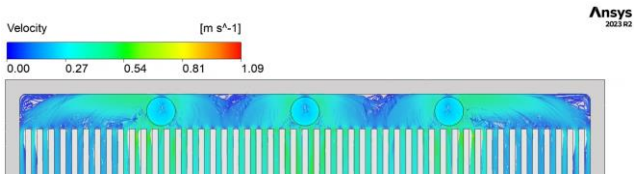

(a). Configuration A

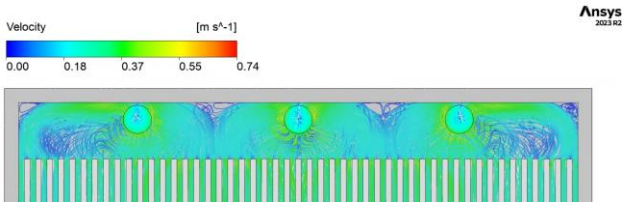

(b). Configuration D

Figure 12: Comparison of flow streamlines in Configuration A and Configuration D

Temperature distribution and sCO_2 temperature variation inside the PCHE channel is demonstrated in Figure 13 for the PCHE with Configuration A (baseline) and Configuration D (proposed) at a mass flow rate of 40 g/sec. Figures 13(a) and 13(b) present the PCHE temperature distribution on the base of the PCHE for configuration A and configuration D correspondingly, while Figures 13(c) and 13(d) display the inlet fluid temperature along the normalized channel length of the two configurations respectively. The temperature distribution is

DOI: 10.17185/duepublico/83329

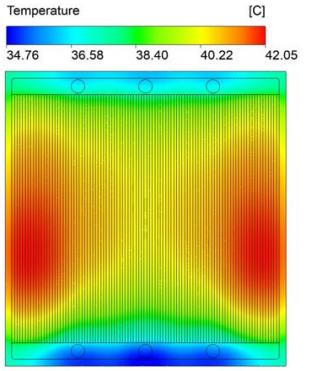

(a). Temperature distribution in Configuration A

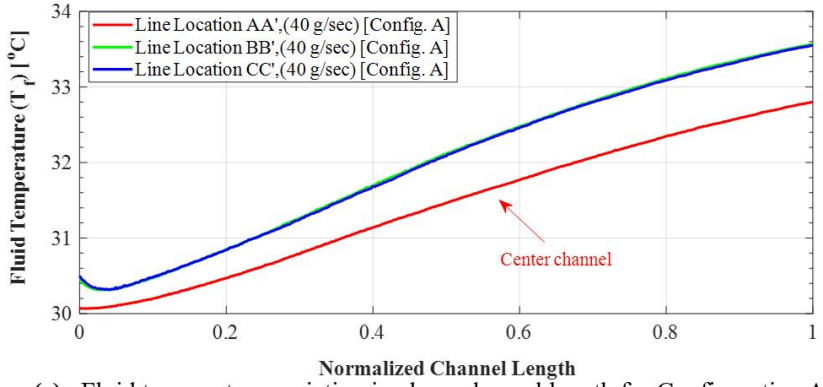

(c). Fluid temperature variation in along channel length for Configuration A

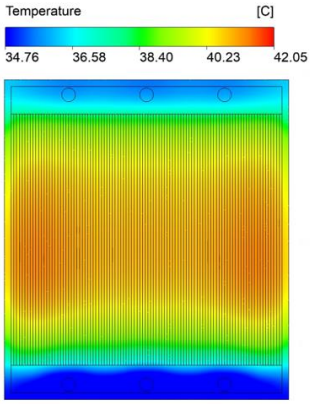

(b). Temperature distribution in Configuration D

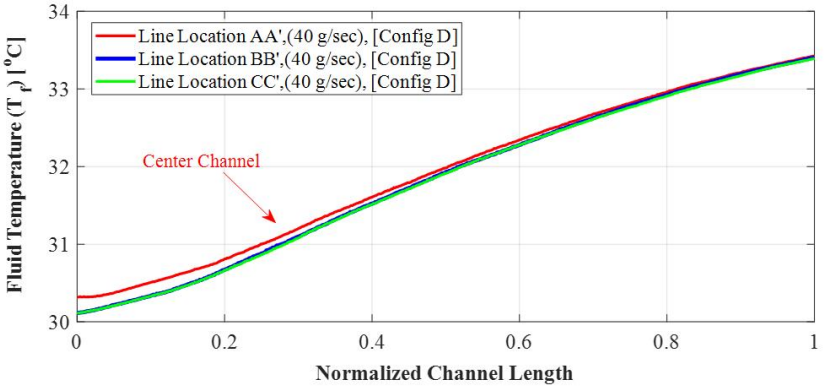

(d). Fluid temperature variation in along channel length for Configuration D

Figure 13: Temperature distribution and fluid temperature variation for baseline and proposed header configuration

presented in Figure 13(b) for Configuration D, which exhibits a markedly improved temperature distribution uniformity compared to Configuration A. The improvement in the design due to an increase in the header area ratio assures a more even flow distribution along the channels and reduces both velocity and temperature gradients. The comparison of fluid temperature profiles for Configurations A and D is shown in Figure 13 (c) and Figure (d). Fluid temperature profiles of channels at locations AA', BB', and CC' for Configuration A show significant divergence as channel AA' which receives high flow rates has the least temperature rise than the other outer channels BB' and CC'. Whereas Figure 13(d) shows closely overlapped temperature profiles for configuration D, due to uniform temperature velocity distribution. The improved temperature uniformity in Configuration D also minimizes the effects of hot and cold stream mixing in the collector headers which can cause significant thermal stress and fatigue over time. Hence, PCHE headers such as Configuration D with optimal inlet configuration can reduce these adverse effects of maldistribution, resulting in a longer life cycle of the PCHE and an increase in its reliability at different operational conditions.

CONCLUSION

This paper investigates the effects of inlet configuration and header area ratio on the flow distribution of a Printed Circuit Heat Exchanger (PCHE) using supercritical CO_2 as working fluid by employing a numerical model. The key findings are summarized as follows:

- Reducing the wall distance for side inlets and increasing the header area ratio significantly reduced the flow maldistribution. Proposed Configuration D with a header area ratio of 10% has the lowest maldistribution factor (MDF), reducing the maldistribution factor by 50.9% as compared to baseline configuration
- The optimized flow distribution with configuration D has ensured uniform fluid temperature profiles across the printed circuit heat exchanger channels and significant reductions in localized hotspots.

It can be concluded from this study that even minor adjustments in inlet and outlet configurations can significantly improve the thermo-hydraulic performance of PCHEs. The scope of this study will be further extended to large-scale PCHEs for industrial applications and different operating conditions.

DOI: 10.17185/duepublico/83329

NOMENCLATURE

c_p	specific heat capacity [J. kg^{-1}. K^{-1}]
d	distance [mm]
H_f	fin height [mm]
h	enthalpy [J]
k	thermal conductivity [$W\ m^{-1}K^{-1}$]
N	number of channels
ΔP	pressure drop [kPa]
P	inlet pressure [MPa]
L	length [mm]
$\boldsymbol{V}$	velocity vector [ms^{-1}]
T	temperature [℃]
W	width [mm]
ρ	density [kg/m^3]
μ	dynamic viscosity [Pas]

Super and subscripts

ch	channel
fl	fluid
HX	Heat Exchanger
HL	Heat load
hd	header
i	inlet
n	normal
sl	solid
t	turbulence

ACKNOWLEDGEMENTS

This work is supported by ISOP Project under Marie Sklodowska-Curie Actions (Grant Agreement No. 1010732266).

REFERENCES

[1] S. hui Liu, Y. ping Huang, J. feng Wang, R. long Liu, and J. guang Zang, "Experimental study of thermal-hydraulic performance of a printed circuit heat exchanger with straight channels," Int J Heat Mass Transf, vol. 160, 2020.

[2] A. A. Awais and M. H. Kim, "Experimental and numerical study on the performance of a minichannel heat sink with different header geometries using nanofluids," Appl Therm Eng, vol. 171, p. 115125, 2020.

[3] H. Li, Y. Zhang, L. Zhang, M. Yao, A. Kruizenga, and M. Anderson, "PDF-based modeling on the turbulent convection heat transfer of supercritical CO_2 in the printed circuit heat exchangers for the supercritical CO_2 Brayton cycle," Int J Heat Mass Transf, vol. 98, pp. 204–218, 2016.

[4] M. Saeed, A. S. Berrouk, M. Salman Siddiqui, and A. Ali Awais, "Numerical investigation of thermal and hydraulic characteristics of sCO_2-water printed circuit heat exchangers with zigzag channels," Energy Convers Manag, vol. 224, 2020.

[5] N. Tsuzuki, Y. Kato, and T. Ishiduka, "High performance printed circuit heat exchanger," Appl Therm Eng, vol. 27, no. 10, pp. 1702–1707, 2007.

[6] D. E. Kim, M. H. Kim, J. E. Cha, and S. O. Kim, "Numerical investigation on thermal-hydraulic performance of new printed circuit heat exchanger model," Nuclear Engineering and Design, vol. 238, no. 12, pp. 3269–3276, 2008.

[7] M. Saeed and M. H. Kim, "Thermal-hydraulic analysis of sinusoidal fin-based printed circuit heat exchangers for supercritical CO_2 Brayton cycle," Energy Convers Manag, vol. 193, pp. 124–139, 2019.

[8] M. Saeed, A. S. Berrouk, M. Salman Siddiqui, and A. Ali Awais, "Effect of printed circuit heat exchanger's different designs on the performance of supercritical carbon dioxide Brayton cycle," Appl Therm Eng, vol. 179, 2020.

[9] J. S. Kwon, S. Son, J. Y. Heo, and J. I. Lee, "Compact heat exchangers for supercritical CO_2 power cycle application," Energy Convers Manag, vol. 209, 2020.

[10] J. Wen, Y. Li, A. Zhou, K. Zhang, and J. Wang, "PIV experimental investigation of entrance configuration on flow maldistribution in plate-fin heat exchanger," Cryogenics (Guildf), vol. 46, no. 1, pp. 37–48, 2006.

[11] S. Kim, "A novel design method of the dividing header configuration using 3D numerical simulation for a heat exchanger with a parallel arrangement," Appl Therm Eng, vol. 159, p. 113807, 2019.

[12] F. A. Tereda, N. Srihari, B. Sunden, and S. K. Das, "Experimental investigation on port-to-channel flow maldistribution in plate heat exchangers," Heat Transfer Engineering, vol. 28, no. 5, pp. 435–443, 2007.

[13] C. C. Wang, K. S. Yang, J. S. Tsai, and I. Y. Chen, "Characteristics of flow distribution in compact parallel flow heat exchangers, part I: Typical inlet header," Appl Therm Eng, vol. 31, no. 16, pp. 3226–3234, 2011.

[14] R. Camilleri, D. A. Howey, and M. D. McCulloch, "Predicting the flow distribution in compact parallel flow heat exchangers," Appl Therm Eng, vol. 90, pp. 551–558, 2015.

[15] W. xiao Chu, K. Bennett, J. Cheng, Y. tung Chen, and Q. wang Wang, "Numerical study on a novel hyperbolic inlet header in straight-channel printed circuit heat exchanger," Appl Therm Eng, vol. 146, pp. 805–814, 2019.

[16] M. Saeed, A. S. Berrouk, M. S. AlShehhi, and Y. F. AlWahedi, "Numerical investigation of the thermohydraulic characteristics of microchannel heat sinks using supercritical CO_2 as a coolant," J Supercrit Fluids, vol. 176, p. 105306, 2021.

[17] F. Jin, D. Chen, L. Hu, Y. Huang, and S. Bu, "Numerical study on flow distribution of supercritical CO_2 in multiple channels of printed circuit heat exchanger," Appl Therm Eng, vol. 234, p. 121185, 2023.

[18] Wolfgang Flaig, Thermohydraulische Untersuchung eines diffusionsgeschweißten

DOI: 10.17185/duepublico/83329

Kompaktwärmeübertragers zur Ertüchtigung eines Wärmeabfuhrsystems mit Kohlenstoffdioxid als Arbeitsmittel, 2019.
[19] S. Patankar, Numerical heat transfer and fluid flow. Taylor & Francis, 1980.
[20] ANSYS CFX, "CFX-Pre user's guide release 23.2," 2023, Ansys Inc., Canonsburg.
[21] T. Dixit and I. Ghosh, "Review of micro- and mini-channel heat sinks and heat exchangers for single phase fluids," Renewable and Sustainable Energy Reviews, vol. 41, pp. 1298–1311, 2015.
[22] M. Kim, H. Jeong, A. Ali Awais, S. Kim, and K. C. Kim, "Experimental and numerical study on the thermal and hydraulic characteristics of porous-media heat exchangers in cryogenic conditions," Appl Therm Eng, vol. 216, p. 119095, 2022.
[23] M. Saeed and M.-H. Kim, "Thermal-hydraulic analysis of sinusoidal fin-based printed circuit heat exchangers for supercritical CO_2 Brayton cycle," Energy Convers Manag, vol. 193, pp. 124–139, 2019.
[24] M. Saeed, A. S. Berrouk, M. Salman Siddiqui, and A. Ali Awais, "Effect of printed circuit heat exchanger's different designs on the performance of supercritical carbon dioxide Brayton cycle," Appl Therm Eng, vol. 179, p. 115758, 2020.
[25] S. G. Kim, Y. Lee, Y. Ahn, and J. I. Lee, "CFD aided approach to design printed circuit heat exchangers for supercritical CO_2 Brayton cycle application," Ann Nucl Energy, vol. 92, pp. 175–185, 2016.
[26] S. M. Lee and K. Y. Kim, "Comparative study on performance of a zigzag printed circuit heat exchanger with various channel shapes and configurations," Heat and Mass Transfer/Waerme- und Stoffuebertragung, vol. 49, no. 7, pp. 1021–1028, 2013.
[27] M. Saeed, A. Ali Awais, and A. S. Berrouk, "CFD aided design and analysis of a precooler with zigzag channels for supercritical CO_2 power cycle," Energy Convers Manag, vol. 236, p. 114029, 2021.
[28] M. Saeed, K. Alawadi, and S. C. Kim, "Performance of Supercritical CO2 Power Cycle and Its Turbomachinery with the Printed Circuit Heat Exchanger with Straight and Zigzag Channels," Energies 2021, Vol. 14, Page 62, vol. 14, no. 1, p. 62, 2020.
[29] E. N. Van Abel Anderson, Mark H., Corradini, Michael L., "Numerical Investigation of Pressure Drop and Local Heat Transfer of Supercritical CO_2 in Printed Circuit Heat Exchangers," S-CO_2 symposium 2011, 2011.
[30] M. Saeed and M. H. Kim, "Thermal-hydraulic analysis of sinusoidal fin-based printed circuit heat exchangers for supercritical CO_2 Brayton cycle," Energy Convers Manag, vol. 193, pp. 124–139, 2019.
[31] M. Saeed and M. H. Kim, "Thermal and hydraulic performance of sCO_2 PCHE with different fin configurations," Appl Therm Eng, vol. 127, pp. 975–985, 2017.
[32] E. Lemmon, M. Mc Linden, and M. Huber, NIST Reference Fluid Thermodynamic and Transport Properties Database: REFPROP Version 9.1, NIST Standard Reference Database 23, 2013.

DOI: 10.17185/duepublico/83329

DuEPublico

Duisburg-Essen Publications online

UNIVERSITÄT DUISBURG ESSEN

Offen im Denken

ub | universitäts bibliothek

Published in: 6th European Conference on Supercritical CO2 (sCO2) for Energy Systems

This text is made available via DuEPublico, the institutional repository of the University of Duisburg-Essen. This version may eventually differ from another version distributed by a commercial publisher.

DOI: 10.17185/duepublico/83329
URN: urn:nbn:de:hbz:465-20250428-114410-7

This work may be used under a Creative Commons Attribution 4.0 License (CC BY 4.0).